Chapter 4
Assessment of SOSM Techniques Applied to Fuel Cells. Case Study: Electric Vehicle Stoichiometry Control

4.1 Introduction

As it was introduced in Chap. 2, the design of proficient control algorithms for the fuel-oxidant coordination problem in PEM fuel cells under variable load operation can reduce the fuel consumption while preventing performance deterioration, oxygen starvation and, eventually, irreversible damage in the polymeric membranes. However, the stoichiometry problem is complex and cannot be successfully tackled by using traditional techniques. A number of reasons turn fuel cell stacks into a major control challenge, e.g. high-order nonlinear equations are required to describe hydrogen-air fed stack dynamics, experimental data-based models usually incorporate look-up tables and piecewise functions, as well as a wide variety of model uncertainties [8]. Besides, many internal variables are inaccessible for measurement, and there exist disturbances that affect the system operation. It is clear that, in order to attain an efficient controller for the FC system, a special control technique capable of coping with such challenges is required.

Therefore, the main objective of this chapter is to evaluate the feasibility of SOSM techniques for oxygen stoichiometry control in PEM fuel-cell-based systems. According to the features reviewed in Chap. 3, SOSM algorithms are especially suited candidates to deal with the aforementioned challenges. In general terms, they are capable of solving the nonlinear robust stability of the fuel cell system, converging to the reference in finite time and avoiding chattering effects, due to the absence of direct discontinuous components in the first derivative of the output. Moreover, if the system is of relative degree 1, then the control action applied to the actual input of the plant will be continuous. Another feature of relevance for fuel cell applications is the control design based on nonlinear models. Given the highly nonlinear nature of the stack, this feature guarantees robust operation and performance in a wider range than those achieved by control methods based on model linearization [8, 9]. In addition, the SOSM control laws are relatively simple, relying on a reduced set of parameters and few measurable variables, rather than on the knowledge of the full state vector. Thus, the implementation requirements and on-line computational burden are considerably alleviated.

The assessment of the SOSM controllers suitability is performed here through computer simulations, using a benchmark model of a fuel cell system for automotive applications. To this end, the model developed by J. Pukrushpan et al. at the Mechanical Department of the Michigan University [8] has been selected, since it is one of the most complete and accurate models available in the open literature (Sect. 4.2). Therefore, the case study under consideration in this chapter is a 75-kW PEM FC stack where the oxygen is fed by an air turbo compressor used in the Ford P2000 fuel cell electric vehicle [8].

4.2 Succinct Description of the Electric Vehicle Fuel Cell System

The first stage in the controllers design procedure is to reformulate the model description according to the design requirements of the SOSM control techniques. A nonlinear state model of the form $\dot{x} = F(x, u, t)$ with F a smooth vector function, at least $\mathscr{C}^1$, is required (see Sect. 4.3). The original benchmark model comprises look-up tables and switched piecewise functions, continuous but not differentiable. Hence, in the proposed design model, they are replaced with smooth functions using adequate polynomial approximations. Additionally, an order reduction based on control considerations of the system physics can be done. Any minor degree of error or uncertainty generated by the aforementioned model adaptation procedure can be added to the inherent uncertainty of the original model. So, such lumped uncertainties, together with external disturbances, are taken into account in the design of the proposed controllers.

Then, the aim of this section is twofold: on the one hand, to present a sixth-order nonlinear state space model of the FC flow system in the SOSM control design form; on the other hand, to review its constituent subsystems, giving a mathematical characterization in accordance with the approach followed for the model construction in [7, 8]. This will be particularly useful to readers unacquainted with such models. However, it is not the intention of this section to give an exhaustive description, but to briefly provide the necessary background to understand the subsequent developments in this book. Therefore, the readers interested in a detailed description and discussions on the benchmark model are referred to the original works of Pukrushpan et al.

The fuel cell generation system (FCGS) roughly comprises five main subsystems: the air flow (breathing), the hydrogen flow, the humidity, the stack electrochemistry and the stack temperature subsystem, respectively. In [8], it is assumed that the input reactant flows are efficiently humidified and the stack temperature is well regulated by dedicated controllers. In addition, it is considered that sufficient compressed hydrogen is available, and therefore the main attention is focused on the air management. In Fig. 4.1 a schematic view of the FCGS under consideration is represented. The most relevant components related to the FC flow system are succinctly characterized in the sequel.
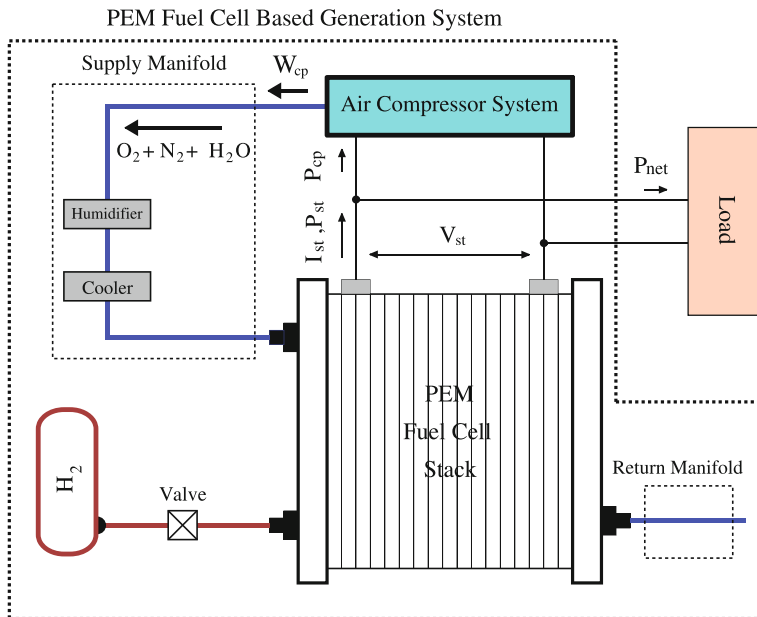
Fig. 4.1 Schematic diagram of a PEM fuel-cell-based generation system (FCGS)

4.2.1 Air Compressor

A 14-kW Allied Signal air turbo compressor is considered in the case under study. Its control input is the command voltage of the DC motor (V_{cp}), while the shaft rotational speed is the only dynamic state variable. The model is divided into two parts. One part is characterized by a static compressor map, which determines the air flow rate through the compressor. The compressor air flow W_{cp} is computed using the rotational speed and the pressure ratio across the compressor. The inlet air is atmospheric, so constant pressure and temperature ($P_{amb} = 1$ atm, $T_{amb} = 25\,°C$) are assumed. The other part represents the dynamics of the air compressor subsystem. Neglecting the armature inductance, a dominant first-order mechanical dynamic equation can be obtained by applying Newton's second law to the rotating parts, assuming lumped rotational parameters:

$$\frac{d\omega_{cp}}{dt} = \frac{1}{J}(T_e - T_l) \tag{4.1}$$

where ω_{cp} is the compressor rotational speed, J is the combined inertia of the compressor motor and the compression device, T_e is the compressor motor torque, and T_l the load torque. T_e can be computed using the simplified DC motor equation

$$T_e = \frac{\eta_{dc}k_{dct}(V_{cp} - k_{dcv}\omega_{cp})}{R_{dc}} \tag{4.2}$$

with k_{dct}, k_{dcv} and R_{dc} the compressor DC motor constants, and η_{dc} its mechanical efficiency.

The load torque T_l depends on the compressor speed, the supply manifold pressure P_{sm}, the compressor efficiency (η_{cp}) and the compressor air flow (W_{cp}). Its expression can be obtained from turbine thermodynamics equations given by [2, 3]

$$T_l = \frac{C_p T_{amb}}{\omega_{cp}\eta_{cp}}\left[\left(\frac{P_{sm}}{P_{atm}}\right)^{\frac{\gamma-1}{\gamma}} - 1\right]W_{cp} \tag{4.3}$$

with C_p the specific heat capacity of air, and γ the ratio of the specific heats of air. W_{cp} is first given as a flow map determined from the pressure ratio across the compressor and the motor shaft speed. Then, the look-up table is replaced by an interpolation given by the Jensen and Kristensen nonlinear curve fitting method [6]. Thus, in the current model, W_{cp} is given in the form of a continuously differentiable bivariate function of P_{sm} and ω_{cp}. In turn, the compressor efficiency was originally represented as a double input look-up table depending on W_{cp} and P_{sm}. However, it has been proved that the use of the mean value of η_{cp} is a sufficiently good approximation for modeling and control design purposes. Under these conditions, the right-hand side of (4.1) is in the whole operation range, at least, a $\mathscr{C}^1$ function.

4.2.2 Air Supply Manifold

The model of the air supply manifold takes into consideration the piping between the compressor and the stack (cooler and humidifier included). Two dynamic equations are required. The first one is given by the mass conservation principle:

$$\frac{dm_{sm}}{dt} = W_{cp} - W_{sm} \tag{4.4}$$

where m_{sm} is the mass of air accumulated in the supply manifold, and W_{cp} and W_{sm} are the manifold inlet and outlet mass flows, respectively. The former comes directly from the compressor subsystem, while the latter, assuming a small pressure gradient between the cathode and the manifold, can be taken as

$$W_{sm} = K_{sm}(P_{sm} - P_{ca}) \tag{4.5}$$

with K_{sm} the supply manifold constant or restriction.

The second dynamic equation results from applying the energy conservation principle and the ideal gas law. Assuming that the air temperature changes inside the manifold, the pressure dynamic equation is given by

$$\frac{dP_{sm}}{dt} = \frac{R_a}{V_{sm}}(W_{cp}T_{cp} - W_{sm}T_{sm}) \tag{4.6}$$

with R_a the gas constant of air, V_{sm} the supply manifold volume, and T_{sm} the manifold air temperature that can be computed using (4.4), (4.6) and the ideal gas law:

$$T_{sm} = \frac{P_{sm}V_{sm}}{m_{sm}R_a} \tag{4.7}$$

4.2.3 Air Humidifier and Temperature Conditioner Subsystems

Typically PEM fuel cell systems require air temperature and humidity conditioning before entering the cathode. According to [8], in this electric vehicle FC stack, the temperature of the air entering the supply manifold is high ($>90\,°C$), and thus it has to be cooled to prevent damage to the fuel cell membranes. Then, it is assumed that an ideal cooler conditions the air temperature to the stack operating temperature ($80\,°C$), without producing an appreciable pressure drop.

Additionally, the cathode air must have a high humidity level to maintain the hydration of the polymeric membranes, but excessive water amounts should be avoided. Dry membrane and flooded fuel cells are both undesirable situations that produce an efficiency reduction and may cause irreversible damage. Hence, in this system a humidifier injects the proper amount of water into the stream, to adjust the cathode inlet flow relative humidity to stay close to 100%. It is assumed that the temperature of the air flow is constant and the humidifier volume is negligible compared to the supply manifold volume.

In order to compute the change in air humidity, due to the additional injection of water, a static model was used. Based on the air flow conditions released by the cooler and by using thermodynamic equations, the mass flows of dry air and vapor can be determined (please refer to [7]). In particular, the vapor saturation pressure of gases is calculated from the flow temperature using the following equation:

$$\log_{10}(P_{sat}) = -1.69 \times 10^{-10}T^4 + 3.85 \times 10^{-7}T^3 \tag{4.8}$$

$$- 3.39 \times 10^{-4}T^2 + 0.143T - 20.92 \tag{4.9}$$

where the units of P_{sat} are [kPa] and [K] for T.

4.2.4 Cathode Channels

The cathode model represents the lumped volume of the cathode channels of the 381 stacked cells. Using the mass conservation principle and thermodynamic properties of the air, the model has been developed under the following assumptions: (1) gases are ideal, (2) the stack and the cathode flow temperatures are constant and uniformly distributed ($80\,°C$), (3) the flow rate of liquid water leaving the cathode is zero, and (4) temperature, pressure, humidity and oxygen mole fraction are equal inside and exiting the cathode. Then, the mass balance of oxygen, nitrogen and water inside the cathode gives

$$\frac{dm_{O_2,ca}}{dt} = W_{O_2,ca,in} - W_{O_2,ca,out} - W_{O_2,react} \tag{4.10}$$

$m_{O_2,ca}$: mass of O_2 inside the cathode.
$W_{O_2,ca,in}$: mass flow rate of O_2 entering the cathode.
$W_{O_2,ca,out}$: mass flow rate of O_2 leaving the cathode.

$W_{O_2,react}$: rate of O_2 reacted.

$$\frac{dm_{N_2,ca}}{dt} = W_{N_2,ca,in} - W_{N_2,ca,out} \tag{4.11}$$

$m_{N_2,ca}$: mass of N_2 inside the cathode.
$W_{N_2,ca,in}$: mass flow rate of N_2 entering the cathode.
$W_{N_2,ca,out}$: mass flow rate of N_2 leaving the cathode.

$$\frac{dm_{w,ca}}{dt} = W_{v,ca,in} - W_{v,ca,out} - W_{v,ca,gen} + W_{v,mem} \tag{4.12}$$

$m_{w,ca}$: mass of water inside the cathode.
$W_{v,ca,in}$: mass flow rate of vapor entering the cathode.
$W_{v,ca,out}$: mass flow rate of vapor leaving the cathode.
$W_{v,ca,gen}$: rate of vapor generated in the fuel cell reaction.
$W_{v,mem}$: mass flow rate of water transferred across the membrane.

The partial pressures of the oxygen, nitrogen and vapor inside the cathode channels can be computed using the ideal gas law for each species.

At this point, an additional analysis can be performed to simplify the cathode model. After a thorough simulation study, it can be established that in this modeled system an important amount of water is transferred across the membrane and, consequently the cathode gas is saturated at almost every operating condition. Therefore, the dynamics of the mass of water inside the cathode ($m_{w,ca}$) can be neglected, turning Eq. (4.12) into an algebraic relationship. Thus, the model dynamics is reduced by one order [4].

4.2.5 Anode Channels

Several assumptions are made in [8] to develop the model of the anode subsystem. The most relevant are: (1) a compressed hydrogen tank and a valve instantaneously ensure sufficient hydrogen flow for the fuel cell reaction, (2) the stack and the anode flow temperatures are the same, (3) one lumped volume is considered, and (4) temperature, pressure and humidity of the hydrogen outlet flow are similar to those of the gas inside the anode channels. In the same way as in the cathode, the gas humidity and partial pressures are computed by balancing hydrogen and water mass flows inside the anode.

$$\frac{dm_{H_2,an}}{dt} = W_{H_2,an,in} - W_{H_2,an,out} - W_{H_2,react} \tag{4.13}$$

$m_{H_2,an}$: mass of H_2 inside the anode.
$W_{H_2,an,in}$: mass flow rate of H_2 entering the anode.
$W_{H_2,an,out}$: mass flow rate of H_2 leaving the anode.

$W_{H_2,react}$: rate of H_2 reacted.

$$\frac{dm_{w,an}}{dt} = W_{v,an,in} - W_{v,an,out} - W_{v,mem} \tag{4.14}$$

$m_{w,an}$: water mass inside the anode.
$W_{v,an,in}$: mass flow rate of vapor entering the anode.
$W_{v,an,out}$: mass flow rate of vapor leaving the anode.
$W_{v,mem}$: mass flow rate of water transfer across the membrane.

In this model the dynamics of the mass of water ($m_{w,an}$) can also be neglected, given that in the model it only affects the hydration of the membrane, which is assumed to be 100% humidified. Then, Eq. (4.14) becomes a static relationship, reducing another order of the model dynamics.

4.2.6 Water Model of the Polymeric Membrane

The hydration model of the membrane allows the computation of the membrane water content and the mass flow rate of water transfer across the membrane. Both are functions of the stack current and the relative humidity of the cathode and anode flows. The dynamics involved in the PEM subsystem are considerably faster than those of the gas channels and the gas diffusion layers, so they have been modeled with static equations. One possible approximation to obtain the membrane water content is to calculate the average between the water content in the anode flow and the cathode flow. On the other hand, the total stack mass flow rate across the membrane ($W_{v,mem}$) depends on two different phenomena: the electro-osmotic drag, i.e. the water molecules dragged across the membrane by the hydrogen proton, and the back diffusion of water from cathode to anode, caused by the concentration gradient [10]:

$$W_{v,mem} = n \cdot A_{fc} \cdot G_v \cdot \left(n_d \frac{i}{F} - D_w \frac{(c_{v,ca} - c_{v,an})}{t_m} \right) \tag{4.15}$$

n: number of fuel cells in the stack.
A_{fc}: fuel cell active area.
G_v: vapor molar mass.
n_d: electro-osmotic drag coefficient.
F: Faraday constant.
D_w: diffusion coefficient of water in the membrane.
$c_{v,ca}$: water concentration in the cathode.
$c_{v,an}$: water concentration in the anode.
t_m: thickness of the membrane.

More details and general ideas about PEM fuel cell modeling can be found in [8] and in Chap. 5 of this book.

4.2.7 Return Manifold

The return manifold model takes into consideration the pipeline dynamics at the fuel cell stack exhaust. The temperature of the air leaving the stack is relatively low (close to 80 °C), so the changes of air temperature in this manifold can be neglected. Therefore, the manifold dynamics follow the isothermic relation

$$\frac{d P_{rm}}{dt} = \frac{R_a T_{rm}}{V_{rm}} (W_{ca,out} - W_{rm,out}) \tag{4.16}$$

P_{rm}: return manifold pressure.
T_{rm}: return manifold temperature.
V_{rm}: return manifold volume.
$W_{ca,out}$: flow entering the return manifold.
$W_{rm,out}$: outlet mass flow of the return manifold.

The relation between the multiple output mass flow, $W_{rm,out}$, and the pressure within its volume, P_{rm}, is modeled through the following piecewise continuous function [8]:

$$W_{rm,out} = \begin{cases} A_1 \cdot P_{rm}(\frac{P_{amb}}{P_{rm}})^{1/\gamma} \cdot [1 - \frac{P_{amb}}{P_{rm}}^{\frac{\gamma-1}{\gamma}}]^{1/2} & \text{if } \frac{P_{amb}}{P_{rm}} > A_2 \\ A_3 \cdot P_{rm} & \text{if } \frac{P_{amb}}{P_{rm}} \leq A_2 \end{cases} \tag{4.17}$$

where A_1, A_2, A_3, P_{amb} and γ are model constants.

Expression (4.17) is not $\mathscr{C}^1$, so it cannot be included in the model for second-order sliding-mode design. Therefore, in order to include the return manifold in the control design model of Sect. 4.3, Eq. (4.17) was replaced by the following fifth-order polynomial [4]:

$$W_{rm,out} = p_0 + p_1 P_{rm} + p_2 P_{rm}^2 + p_3 P_{rm}^3 + p_4 P_{rm}^4 + p_5 P_{rm}^5 \tag{4.18}$$

The values of the polynomial constants in Eq. (4.18) can be found in Appendix A, Table A.1.

4.3 Electric Vehicle FCGS State Space Model for SOSM Control Design

To conclude the first stage of the control design procedure, the dynamic equations required for oxygen stoichiometry control must be rearranged in the SOSM design form. Considering that in this model the anode subsystem is decoupled from the cathode subsystem and does not enter in the oxygen stoichiometry control loop, its dynamics can be neglected, and the system order is reduced by one.

As a result of the reduction and rebuilding work performed on Pukrushpan et al.'s model, the following sixth-order control design model is proposed:

$$\dot{x} = F(x, u, t) = f(t, x) + g(t, x, u)$$
$$x \in \mathbb{R}^6; \quad u \in \mathbb{R}; \quad f : \mathbb{R}^6 \to \mathbb{R}^6; \quad g : \mathbb{R}^6 \to \mathbb{R}^6 \tag{4.19}$$

with f and g sufficiently smooth vector functions, where the coordinates of the state vector

$$x = [\omega_{cp} \quad P_{sm} \quad m_{sm} \quad m_{O_2,ca} \quad m_{N_2,ca} \quad P_{rm}]^T \qquad (4.20)$$

can be summarized as follows:

- $x_1 = \omega_{cp}$: angular speed of the compressor motor that feeds the stack cathode through the supply manifold.
- $x_2 = P_{sm}$: total pressure inside the supply manifold, consisting of the sum of the partial pressures of the gases that constitute the air (oxygen, nitrogen and water vapor).
- $x_3 = m_{sm}$: total mass of air in the supply manifold, consisting of the sum of the instantaneous masses of oxygen, nitrogen and water vapor.
- $x_4 = m_{O_2,ca}$: instantaneous oxygen mass in the stack's cathode channels. This state is affected by the oxygen consumed in the reaction, the amount of oxygen coming from the supply manifold and the oxygen mass outgoing through the return manifold.
- $x_5 = m_{N_2,ca}$: instantaneous mass of nitrogen inside the stack's cathode channels. It only relies on the incoming nitrogen from the supply manifold and the outgoing nitrogen that leaves the stack through the return manifold.
- $x_6 = P_{rm}$: total pressure inside the return manifold, consisting of the sum of the partial pressures of the gases that constitute the air.

The input $u(t)$ is the normalized input voltage of the compressor DC motor V_{cp}. The normalization constant ($V_{nor} = 180$ V) is the maximum value of V_{cp} in the operating region.

The detailed expressions of the system model are given by

$$
\begin{aligned}
\dot{x}_1 =\ & B_3 n(x)\big(1 - d(x)\big) + \big(B_1 u^2 x_1^{-1} - B_2 u\big) \\
\dot{x}_2 =\ & B_6\big(1 - d(x)\big)x_1\big(1 + n(x)n_{cp}^{-1}\big) - \big(x_2^2 B_7 - x_2 B_8 - x_2 x_5 B_9 - x_2 x_4 B_{10}\big)x_3^{-1} \\
\dot{x}_3 =\ & B_{11}\big(1 - d(x)\big)x_1 - x_2 B_{12} + B_{13} + x_5 B_{14} + x_4 B_{15} \\
\dot{x}_4 =\ & \big((x_2 B_{59} - B_{60} - x_5 B_{61} - x_4 B_{62})(x_2 - x_2 B_{21})^{-1} e(x) \\
& + (x_2 B_{63} - B_{64} - x_5 B_{65} - x_4 B_{66})e(x)\big)k(x) - x_4(B_{25} + x_5 B_{26} \\
& + x_4 B_{27} - x_6 B_{24})j(x)x_4^{-1}\big(j(x)B_{67} + G_{N_2}\big)^{-1} m(x) - I_{st} B_{32} \qquad (4.21) \\
\dot{x}_5 =\ & \big((x_2 B_{50} - B_{51} - x_5 B_{52} - x_4 B_{53})(x_2 - x_2 B_{21})^{-1} e(x) + (x_2 B_{54} \\
& - B_{55} - x_5 B_{56} - x_4 B_{57})e(x)\big)k(x) - \big(1 - j(x)B_{30}\big(j(x)B_{68} + G_{N_2}\big)^{-1}\big) \\
& \times (B_{35} + x_5 B_{36} + x_4 B_{37} - x_6 B_{34})m(x) \\
\dot{x}_6 =\ & B_{47} + x_5 B_{48} + x_4 B_{49} - x_6 B_{46} - B_{39}c(x)^5 - B_{40}c(x)^4 - B_{41}c(x)^3 \\
& - B_{42}c(x)^2 - B_{43}c(x) - B_{44}
\end{aligned}
$$

with the auxiliary functions

$$
\begin{aligned}
a(x) &= a_1(x) + a_{21}(x)a_{22}(x)x_1 \\
a_1(x) &= 1 - d(x) \\
a_{21}(x) &= d(x) \\
a_{22}(x) &= -2B_{69}x_1^{-3}n(x) \\
b(x) &= b_1(x)b_2(x)x_1 \\
b_1(x) &= a_{21}(x) \\
b_2(x) &= \frac{B_{69}B_4x_2^{B_4-1}}{x_1^2 P_{amb}^{B_4}} \\
c(x) &= x_6 - B_{45} \\
d(x) &= e^{B_{69}\left(\left(\frac{x_2}{P_{amb}}\right)^{B_4}-1\right)x_1^{-2}-\beta} \\
e(x) &= \left(1 + \frac{x_2 B_{20}}{x_2 - x_2 B_{21}}\right)^{-1} \\
j(x) &= \frac{x_4}{x_5 B_{28} + x_4 B_{29}} \\
k(x) &= \left(1 + \frac{B_{22}}{x_2 - x_2 B_{21} + B_{23}}\right)^{-1} \\
m(x) &= \left(1 + B_{58}\left(j(x)B_{68} + G_{N_2}\right)^{-1}j(x)x_4^{-1}\right)^{-1} \\
n(x) &= \left(\frac{x_2}{P_{amb}}\right)^{B_4} - 1
\end{aligned}
\tag{4.22}
$$

The compressor air flow can be written in terms of the states as follows:

$$
W_{cp} = B_{11}\left(1 - d(x)\right)x_1 \tag{4.23}
$$

The constants are given in Appendix A, Table A.2.

4.4 Control Objective and Sliding Surface

The second stage in the SOSM control design procedure is to establish the control objective and, accordingly, define the sliding surface. In this case, the proposed objective is the optimization of the energy conversion of the FCGS, maximizing the net power (P_{net}) generated by the system under different load conditions. We assume that the system net power results as follows:

$$
P_{net} = P_{st} - P_{cp} \tag{4.24}
$$

P_{st}: stack generated power.
P_{cp}: compressor power demand.

It can be shown that the efficiency optimization can be achieved by regulating the oxygen mass flow entering to the stack cathode. If an adequate comburent flow is
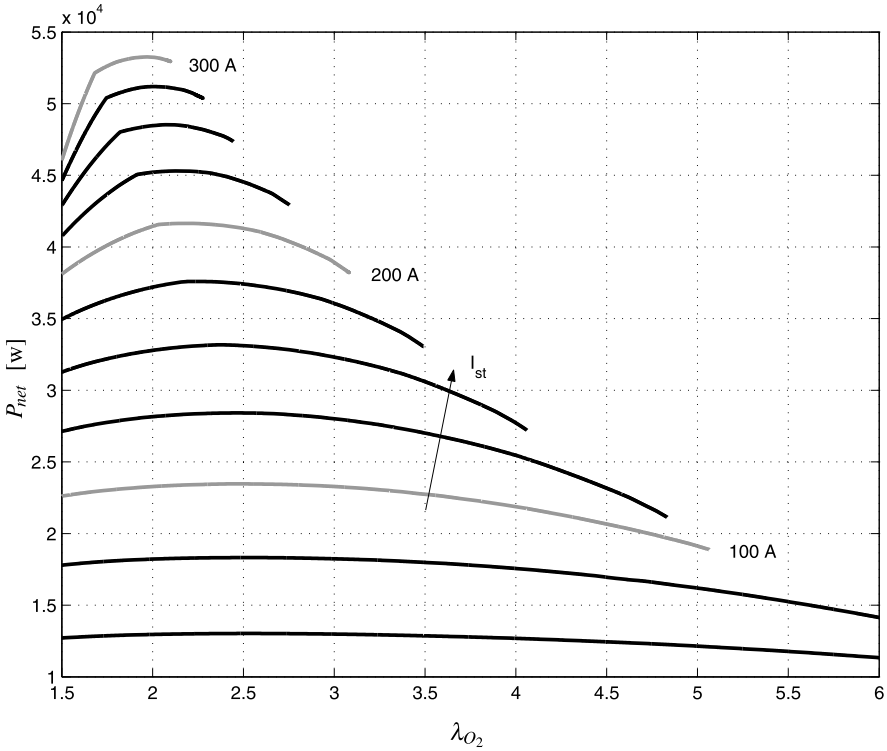
Fig. 4.2 Steady state analysis of the system performance under different load conditions

ensured through the stack, the load demand is satisfied with minimum fuel consumption. Additionally, oxygen starvation and irreversible membrane damage are averted.

Accomplishing such an optimal comburent flow is equivalent to maintaining the oxygen excess ratio of the cathode at an optimal value. The oxygen excess ratio or oxygen stoichiometry is defined as

$$\lambda_{O_2} = \frac{W_{O_2,ca,in}}{W_{O_2,react}} \tag{4.25}$$

where $W_{O_2,ca,in}$ is the aforementioned oxygen partial flow entering the cathode, which depends on the air flow released by the compressor W_{cp}. Recall that $W_{O_2,react}$ is the oxygen flow consumed in the reaction, so it is directly related to the stack current:

$$W_{O_2,react} = G_{O_2} \frac{nI_{st}}{4F} \tag{4.26}$$

with G_{O_2} the molar mass of oxygen.

The optimum value of λ_{O_2} is determined from a thorough off-line analysis of the open-loop system, considering changes in the current demand and a wide range of oxygen stoichiometry values. In Fig. 4.2 it can be observed that the optimum

value of λ_{O_2} ($\lambda_{O_2,opt}$) depends on I_{st}. However, in the electric vehicle FCGS under consideration, $\lambda_{O_2,opt}$ presents minor variations over the operation range. Therefore, a constant value of $\lambda_{O_2,opt}$ was used when computing the system reference. This condition may not hold for other PEM fuel cell systems, and hence the variable $\lambda_{O_2,opt}$ could be easily expressed as a function of I_{st}. Alternatively, a possible solution would be to apply an extremum seeking algorithm. In that case, the proposed problem is solved by a local minimum algorithm, which does not rely on a detailed model description, and it is considered as a nonlinear on-line optimization for unconstrained problems [1].

Another important advantage of stoichiometry control is the avoidance of oxygen starvation on the cathode channels, which would occur if λ_{O_2} is allowed to go below 1. Oxygen starvation represents a significant problem in PEM fuel cell systems because if it persists for a long time, it may produce hot spots and consequent irreversible damage in the catalyst layers and polymeric membranes.

Once $\lambda_{O_2,opt}$ is determined, the objective of keeping the oxygen excess ratio within optimal values can be written in terms of controlling the oxygen mass flow ($W_{O_2,ca,in}$). Then, the following cathode oxygen mass flow reference can be obtained from (4.25) and (4.26):

$$W_{O_2,ca,ref} = \lambda_{O_2,opt} G_{O_2} \frac{n I_{st}}{4F} \tag{4.27}$$

where tracking $W_{O_2,ca,ref}$ effectively implies $\lambda_{O_2} = \lambda_{O_2,opt}$.

Nevertheless, due to the fact that $W_{O_2,ca,in}$ is an inaccessible internal variable of the FCGS, it is not practical to include it in the control algorithm. This problem can be successfully circumvented by inferring information of $W_{O_2,ca,in}$ from an accessible variable of the system, such as the air mass flow delivered by the turbo compressor (W_{cp}). Under the aforementioned fixed humidification assumption, this variable is directly related to $W_{O_2,ca,in}$ through the supply manifold dynamics. Furthermore, once the manifold transient is finished, the relation between W_{cp} and $W_{O_2,ca,in}$ remains fixed in all operating conditions. Therefore, the operation of the stack close to its maximum efficiency points can be successfully achieved by posing the control objective in terms of a tracking control problem of W_{cp} (in this way, $\lambda_{O_2} = \lambda_{O_2,opt}$ is ensured for every load condition, once the supply manifold transient expires) [5].

As it has been reviewed in Chap. 3, in the framework of the sliding-mode theory, such a control objective is formalized defining the sliding variable

$$s(x,t) = W_{cp} - W_{air,ref} \tag{4.28}$$

and steering s to zero. The expression of the air mass flow reference $W_{air,ref}$ can be readily obtained from the cathode oxygen mass flow reference (4.27). Given that the molar fraction of oxygen in the air is known ($\chi_{O_2} = 0.21$), the desired mass flow of dry air can be directly computed from (4.26):

$$W_{dry,ref} = \frac{1}{\chi_{O_2}} W_{O_2,ca,ref} = \frac{1}{\chi_{O_2}} \lambda_{O_2,opt} G_{O_2} \frac{n I_{st}}{4F} \tag{4.29}$$

Then, taking into account the relative humidity of the air (RH_{amb}), the final expression of the air mass reference results in

$$W_{air,ref} = (1 + \omega_{amb}) \frac{1}{\chi_{O_2}} \lambda_{O_2,opt} G_{O_2} \frac{n I_{st}}{4F} \tag{4.30}$$

ω_{amb} being the rate of vapor in the ambient air flow,

$$\omega_{amb} = \frac{G_v}{G_a} \frac{P_{sat}(T_{amb}) RH_{amb}}{P_{amb} - P_{sat}(T_{amb}) RH_{amb}} \tag{4.31}$$

G_a: molar mass of dry air.
G_v: molar mass of vapor.

Note that for stable ambient conditions, the reference $W_{air,ref}$ only depends on one single measurable variable, the stack current (I_{st}).

4.5 Design of a SOSM Super-Twisting Controller for the Electric Vehicle FCGS

Once the FCGS dynamic model has been re-modeled in the SOSM design form and the sliding variable s has been defined, the final stage of the design procedure, i.e. the synthesis of the SOSM control law, can be completed in terms of $\lambda_{O_2,opt}$ and the measurable system variables W_{cp} and I_{st}.

According with the SOSM design procedure presented in Chap. 3, the controller design requires the computation of the time derivative of s and global bounds for the second derivative. To this end, using (4.23) and (4.28), we can write the sliding variable as

$$s(x,t) = W_{cp} - W_{air,ref}$$
$$= B_{11}(1 - d(x))x_1 - (1 + \omega_{amb}) \frac{1}{\chi_{O_2}} \lambda_{O_2,opt} G_{O_2} \frac{n I_{st}}{4F} \tag{4.32}$$

and directly derive, through standard mathematical computations, the expressions of the first and second time derivatives of s:

$$\dot{s}(x,t) = \frac{\partial}{\partial t} s(x,t) + \frac{\partial}{\partial x} s(x,t).\big(f(x,t) + g(x,u,t)\big) \tag{4.33}$$

$$\ddot{s}(x,t) = \frac{\partial}{\partial t} \dot{s}(x,t) + \frac{\partial}{\partial x} \dot{s}(x,t).\big(f(x,t) + g(x,u,t)\big)$$
$$+ \frac{\partial}{\partial u} \dot{s}(x,t).\dot{u}(t) = \varphi(x,u,t) + \gamma(x,u,t)\dot{u}(t) \tag{4.34}$$

The vector fields f and g are smooth enough in the stack operation range, and information about s is assumed to be available. Besides, note that s does not explicitly depend on the control input, but u does appear in $\dot{s}$ via the expression of $\dot{x}_1$; consequently, the sliding variable s has relative degree 1 with respect to u.

Then, analyzing the system equations, it is verified that the conditions required for SOSM control design are satisfied by the fuel cell system model (4.19) with output s given by (4.32). In accordance with the general framework established in Chap. 3, the system is under the conditions established in Case 1 of Sect. 3.5.1, which for the particular FCGS under study are:

1. Given the total second time derivative $\ddot{s}$, there are bounds Γ_m and Γ_M such that, within the region $|s(x, t)| < s_0$, the following inequality holds for all $t, x \in \mathcal{X}$, $u \in \mathcal{U}$:

$$0 < \Gamma_m \leq \gamma(x, u, t) = \frac{\partial}{\partial u}\dot{s}(x, t) \leq \Gamma_M \qquad (4.35)$$

   For the fuel cell stack under consideration, such bounds were obtained from a detailed analysis of the system structure together with comprehensive simulation studies, considering the addition of an appropriate feedforward control that leads the system to the validity region. As a result, the following bounds were determined for $s_0 = 5e^{-3}$:

$$\Gamma_m = 0.5, \qquad \Gamma_M = 0.9$$

2. Analogously, a positive constant ($\Phi = 0.01$ for this FCGS) can also be calculated, such that, within the region $|s| < s_0$, the following inequality holds for all $t, x \in \mathcal{X}, u \in \mathcal{U}$:

$$\left| \frac{\partial}{\partial t}\dot{s}(x, t) + \frac{\partial}{\partial x}\dot{s}(x, t).\big(f(x, t) + g(x, u, t)\big) \right| \leq \Phi \qquad (4.36)$$

   with I_{st} covering the whole operation range of the stack (1 A to 300 A).

   Therefore, the stabilization problem of the electric vehicle FCGS (4.19) with input–output dynamics (4.34) is solved through the solutions of the following equivalent differential inclusion by applying SOSM:

$$\ddot{s} \in [-\Phi = -0.01, \Phi = 0.01] + [\Gamma_m = 0.5, \Gamma_M = 0.9]\dot{u} \qquad (4.37)$$

and the final parameters of the robust controller can be designed based on Φ, Γ_m and Γ_M.

   It is interesting to stress that the bounds for functions $\varphi(x, u, t)$ and $\gamma(x, u, t)$ were calculated considering the bounded perturbations and uncertainties existing in the FCGS. In this way, (4.37) covers their effects, and hence the design based on these values results in controllers which are naturally robust to such disturbances.

   In the sequel, a control law based on the *Super-Twisting* (ST) algorithm is developed. As it was explained in Chap. 3, this algorithm only requires the knowledge of the sign of s during on-line operation, and it is specially suited for plants of relative degree 1, like the FC system under consideration. According to (3.93) and (3.94), the control u is given as the sum of two components:

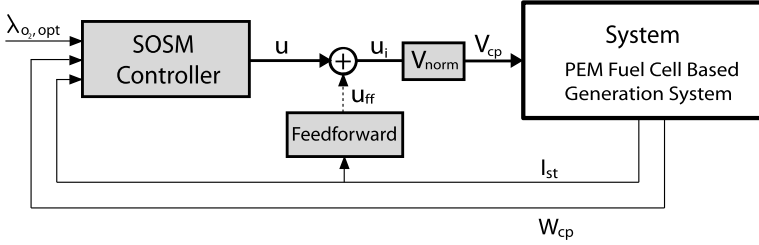$$u(t) = u_1(t) + u_2(t) \qquad (4.38)$$

Fig. 4.3 Schematic block diagram of the FCGS and the proposed SOSM control set up

$$\dot{u}_1(t) = -\alpha\,\mathrm{sign}(s)$$
$$u_2(t) = -\lambda|s|^{\rho}\,\mathrm{sign}(s) \tag{4.39}$$

where the controller parameters γ, λ and ρ are designed to fulfill the sufficient conditions for convergence to $s(x) = \dot{s}(x) = 0$ in finite time, i.e.

$$\alpha > \frac{\Phi}{\Gamma_m}$$
$$\lambda^2 > \frac{2}{\Gamma_m^2}\frac{(\Gamma_m\alpha + \Phi)^2}{(\Gamma_m\alpha - \Phi)} \tag{4.40}$$
$$\rho = 0.5$$

In this way it is ensured that the control has sufficient authority to affect the sign of $\ddot{s}$, guaranteeing the establishment of a SOSM.

To complete the control set up to be implemented, as previously mentioned, an appropriate extra control action is added, to steer the sliding variable within the validity region. In the FCGS, a feedforward action (u_{ff}) proved to be effective to speed up the reaching phase. Therefore, u_{ff} was included into the control scheme, and the implemented control action ($u_i(t)$) comprises two terms:

$$u_i(t) = u(t) + u_{ff}(t) \tag{4.41}$$

where u corresponds to the SOSM control action particularized by Eqs. (4.38) and (4.39). The expression of u_{ff} is computed via a simple polynomial, a function of the measurable current I_{st}, obtained from an off-line test along the entire operation range of the FCGS [8].

A schematic block diagram of the control set-up proposed for implementation can be appreciated in Fig. 4.3.

To refine the final tuning of the Super-Twisting controller, it is recommended to consider not only the behavior of the controlled variable (in this case the oxygen stoichiometry), but also any other involved variable that can affect the overall performance of the plant. For instance, in this particular system, the electric quality of the FCGS net power should be also taken into account. This is due the direct effect of the control on the electric power (a relative degree 0 output). Therefore, the Super-Twisting controller parameters were selected aiming to smooth the control

Table 4.1 Variations of system parameters

Parameter	Variation
Stack temperature (T_{st})	$+10\%$
Cathode volume (V_{ca})	$+5\%$
Supply manifold volume (V_{sm})	-10%
Atmospheric pressure (P_{atm})	$+10\%$
Ambient temperature (T_{amb})	$+10\%$
Return manifold volume (V_{rm})	-10%
Motor constant (K_v)	-10%
Electric resistance of the motor (R_{cm})	$+5\%$
Compressor diameter (d_c)	$+1\%$
Motor inertia (J)	$+10\%$

action and to have a low content of high-frequency components. After an iterative refining procedure, the most adequate set of parameters resulted as follows:

$$\alpha = 2, \qquad \lambda = 3, \qquad \rho = 0.5 \tag{4.42}$$

In the next section it will be shown that, under the influence of the control (4.41), the phase portrait (($s, \dot{s}$) plane) of the controlled system presents the characteristic non-monotonous behavior of the homogeneous Super-Twisting algorithm. The trajectories converge to the origin in finite time, twisting around the center during the reaching mode.

4.6 SOSM Super-Twisting Controller Simulation Results

To evaluate the efficiency of the proposed controller (4.41) dealing with model uncertainties, external disturbances and a wide range of current demand, a number of simulation studies were performed. To assess the SOSM controller performance under realistic operating conditions, simulation tests were conducted using the comprehensive ninth-order nonlinear model developed in [8]. The simulation model incorporates the original look-up tables representing parameter characteristics obtained from experimental data. In addition, extra uncertainty has been incorporated in several parameters of the system (see Table 4.1).

Moreover, an unknown torque disturbance, modeled as a noisy quadratic function of the angular speed (ω_{cp}), was included in the same test (see Fig. 4.4). This friction term is set to start at $t = 15$ sec, and its expression is

$$T_p = \omega_{cp}(t)^2 B_1 + \omega_{cp}(t) B_2 + e(t) \tag{4.43}$$

with $B_1 = 10^{-9}$ [N m/s^2], $B_2 = 20 \times 10^{-6}$ [N m/s] and $e(t)$ corresponding to a band-limited noise component.

Then, the features of the designed controller are examined through simulation tests, which aim to demonstrate its nominal performance and its robust tracking
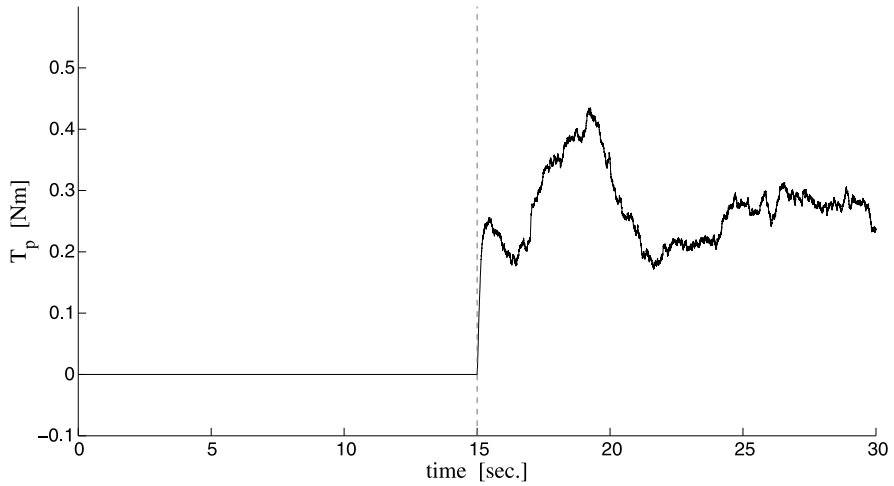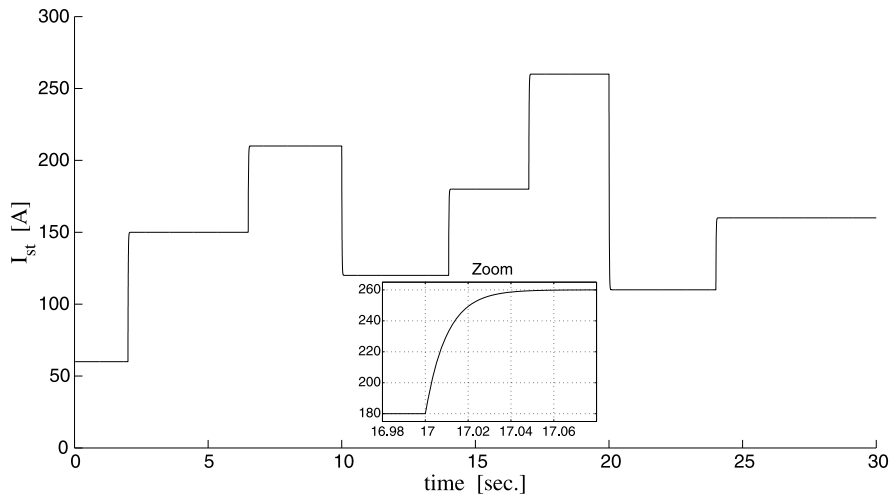
Fig. 4.4 Torque disturbance

Fig. 4.5 Load current

characteristics in the presence of the aforementioned unknown disturbances and uncertainties. To this end, series of load current (ranging from 60 A to 300 A) were designed in order to illustrate the air regulation performance in a wide range of operation. The sequence of current variations, generated from a filtered steps series, is shown in Fig. 4.5. Note that abrupt and significant changes in the amplitude of the load demand were considered to test the proficiency of the controller under exacting operating conditions.
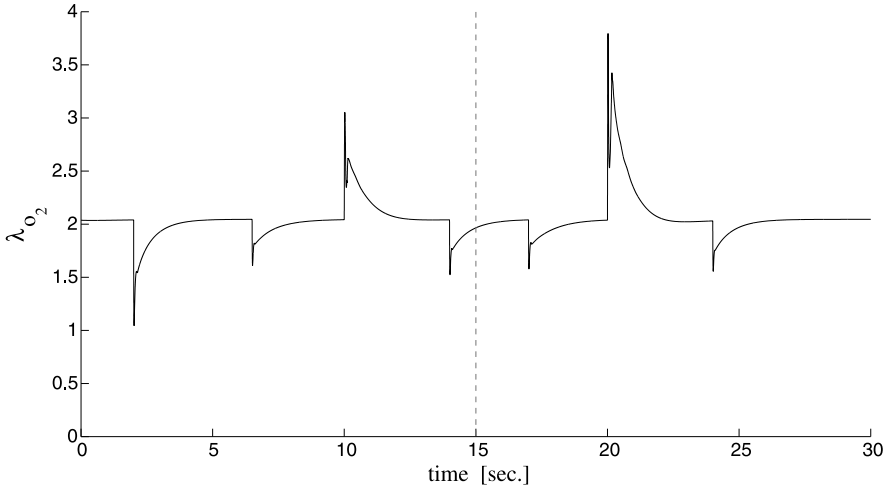
Fig. 4.6 Oxygen excess ratio (oxygen stoichiometry)

In Fig. 4.6 and the sequel, the black line depicts the system variables evolution in the presence of uncertainties and friction disturbances, while the grey line shows the corresponding variables of the undisturbed system. Note that in Figs. 4.6, 4.8 and 4.9 both lines are superimposed during the entire test.

The behavior of the oxygen stoichiometry (λ_{O_2}) under different load conditions is depicted in Fig. 4.6. In accordance with the explanation of Sect. 4.4, the values of λ_{O_2} that enable the system to work in its maximum net power points were determined performing off-line simulations (Fig. 4.2). In this electric vehicle FCGS, due to the relatively small variation of $\lambda_{O_2,opt}$ for different values of stack current, a unique value $\lambda_{O_2,opt} = 2.05$ was adopted. When $\lambda_{O_2,opt}$ is reached, it can be assured that the system is working in the neighborhood of its maximum power generation points. It is observed in Fig. 4.6 that the excess oxygen ratio satisfactorily follows that reference in spite of uncertainties and disturbances.

Figures 4.7 and 4.8 present the dynamic behavior of the system net power (P_{net}) and the stack voltage (V_{st}). It can be observed that, effectively, the former displays a desirable low content of high-frequency components. Besides, remark that the noticeable difference between the net power of the nominal and the disturbed system (after $t = 15$ sec) is not a controller flaw, but the expected consequence of the addition of the torque disturbance of Fig. 4.4. To compensate this spurious load, the compressor must increase its consumption, hence for given I_{st}, the resultant net power decreases. In spite of all disturbances, the ST robustly controls the output s, as attested by Fig. 4.9.

Figure 4.9 shows the evolution of the sliding output s. Once the brief reaching mode elapses, the controller maintains the system operating on the sliding surface ($s = 0$, i.e. regulating λ_{O_2} at its optimum value), despite the coexistence of parameters uncertainties, external perturbations and important load variations. Recall that
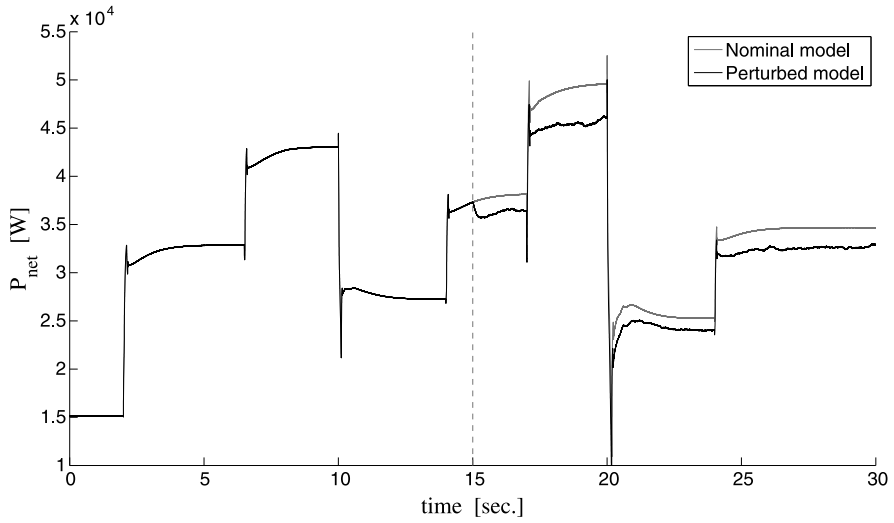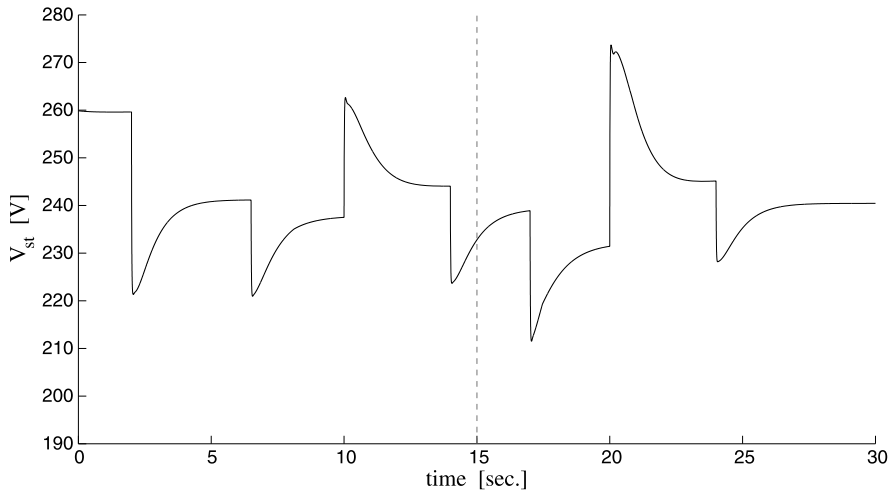
Fig. 4.7 Net power delivered by the system

Fig. 4.8 Stack output voltage

the stability of the closed-loop system is guaranteed because the differential inclusion (4.37) has been computed to hold in the presence of such disturbances.

Note that s exhibits the typical overshoots of a system controlled by an ST algorithm (Fig. 4.9). Effectively, the characteristic twisting behavior imposed by the Super-Twisting controller can be better appreciated in Fig. 4.10, where the phase portrait of the system is plotted for a representative lapse, ranging in time from 24.2 sec to 24.3 sec.
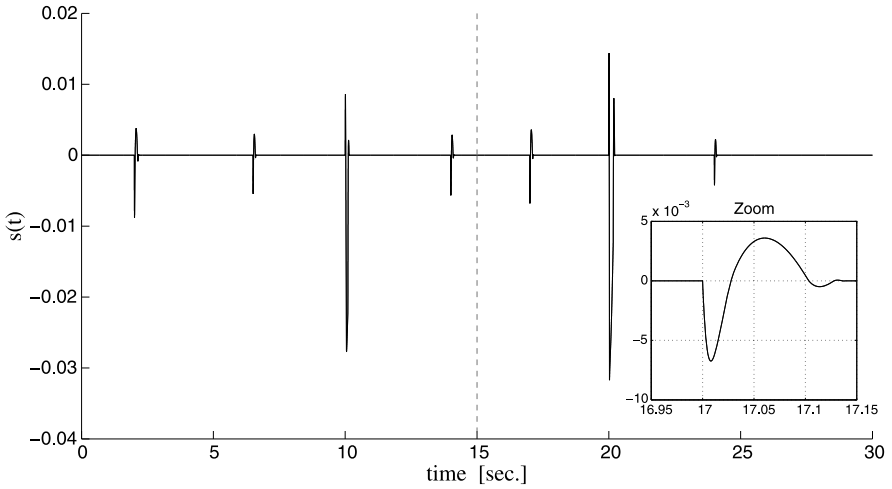
Fig. 4.9 Sliding variable
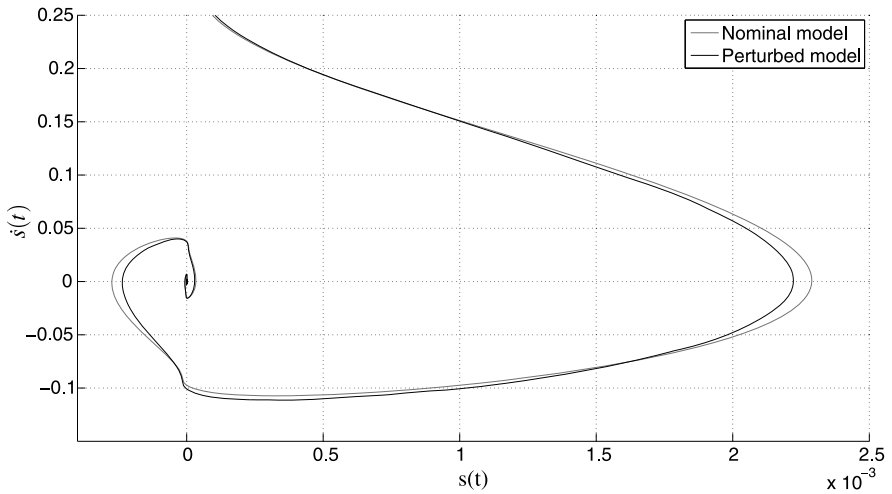
Fig. 4.10 s vs. $\dot{s}$

Finally, in Fig. 4.11 the time evolution of the control signals are presented, in terms of the actual input compressor voltage units (i.e. denormalizing the control actions by multiplying by V_{nor}). The implemented control action u_i that drives the fuel-cell-based system, together with the two constituent components u and u_{ff}, are depicted. Note the increase in the control effort after the appearance of the friction disturbance. To counteract its effect, the SOSM controller is in charge of providing the necessary action to achieve the regulation objective.
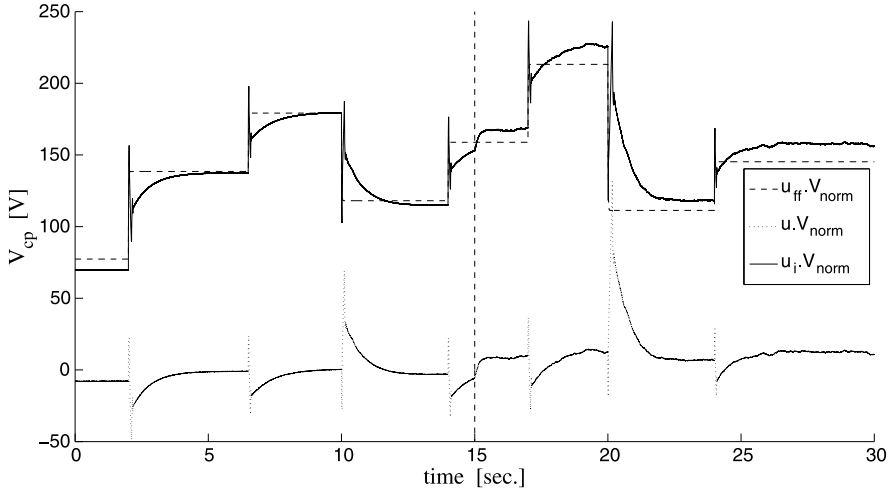
Fig. 4.11 Control signal

4.7 Comparison with Other Control Strategies

4.7.1 Different SOSM Control Algorithms

In this section, the electric vehicle FCGS performance is evaluated under the action of other control algorithms. Given the encouraging results obtained in the previous section that proved the suitability of a SOSM ST controller for oxygen stoichiometry control, it is naturally of interest to explore the capabilities of other SOSM algorithms. Therefore, two SOSM controllers based on Twisting and Sub-Optimal algorithms, respectively, are synthesized and assessed in the present subsection. According to the description in Chap. 3, these SOSM algorithms are originally intended for relative degree 2 systems, and thus the FCGS must be expanded with an integrator, taking the ancillary input $v = \dot{u}(t)$ as the control action for the design (see Fig. 4.12).

4.7.1.1 Twisting Algorithm

As it was previously established, the *Twisting* controller is given by

$$v = \dot{u} = -r_1 \operatorname{sign}(s) - r_2 \operatorname{sign}(\dot{s}) \tag{4.44}$$

with sufficient conditions for finite-time convergence

$$\begin{aligned}
& r_1 > r_2 > 0 \\
& (r_1 + r_2)\Gamma'_m - \Phi' > (r_1 - r_2)\Gamma'_M + \Phi' \\
& (r_1 - r_2) > \frac{\Phi'}{\Gamma'_m}
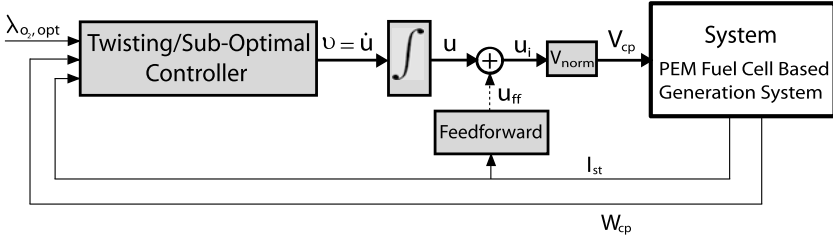\end{aligned} \tag{4.45}$$

Fig. 4.12 Schematic block diagram proposed for Twisting and Sub-Optimal algorithms in relative degree one systems

Note that the control law (4.44) requires the knowledge of s and $\dot{s}$ and, in the relative degree 1 fuel cell system, synthesizes a continuous control voltage V_{cp}, due to the integrator.

Recall that in this particular case, in which the relative degree 2 system is artificially obtained from expanding a relative degree 1 plant, the bounds of the former are equal to those of the latter (see Chap. 3, Sect. 3.5.2.1). Therefore, the *Twisting* controller gains can be directly computed using the same bounds calculated in (4.35) and (4.36) (i.e., $\Gamma_m' = \Gamma_m = 0.5$, $\Gamma_M' = \Gamma_M = 0.9$ and $\Phi' = \Phi = 0.9$). Then, the selected parameters for the controller were $r_1 = 2.25$ and $r_2 = 0.75$.

4.7.1.2 Sub-Optimal Algorithm

The *Sub-Optimal* control law, detailed in Chap. 3, is given by

$$
\begin{aligned}
v = \dot{u} &= -\alpha(t)U \, \mathrm{sign}(s - \beta s_M) \\
\alpha(t) &= \begin{cases} 1 & \text{if } (s - \beta s_M)s_M \geq 0 \\ \alpha^* & \text{if } (s - \beta s_M)s_M < 0 \end{cases}
\end{aligned}
\tag{4.46}
$$

It requires the knowledge of s and of the last extremal value of the sliding variable, s_M, that is the value of s at the last local maximum, minimum or horizontal inflexion point, which has to be updated on-line (see Chap. 3, Sect. 3.5.2.3 for details). To ensure the finite-time convergence, the minimum control magnitude $U > 0$, the modulation factor $\alpha^* > 1$ and the anticipation factor $0 \leq \beta < 1$ must be selected in accordance with

$$
\begin{aligned}
U &> \frac{\Phi'}{\Gamma_m'} \\
\alpha^* &\in [1; +\infty) \cap \left[\frac{\Phi' + (1 - \beta)\Gamma_M' U}{\beta \Gamma_m' U}; +\infty \right)
\end{aligned}
\tag{4.47}
$$

Then, the Sub-Optimal controller parameters for the electric vehicle fuel cell were chosen as $U = 3$, $\beta = 0.3$ and $\alpha^* = 5$.
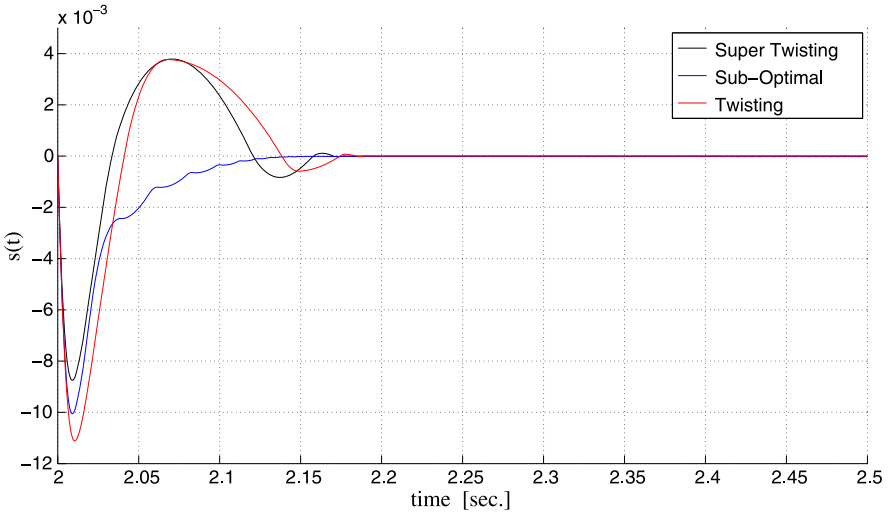
Fig. 4.13 Time evolution of the sliding variable under the action of different SOSM controllers

4.7.1.3 SOSM Comparison Simulation Tests

To assess and compare the performance of the aforementioned SOSM controllers, simulation tests start considering the undisturbed FCGS, and, later, several sources of disturbances are incorporated. Similarly to the Super-Twisting case, in Sect. 4.6, the complete ninth-order nonlinear model developed in [8] is used to model the plant in the simulations. Additionally, the same load profile utilized in Sect. 4.6 is used for these tests (see stack drained current in Fig. 4.5).

Results of the three SOSM algorithms (namely Super-Twisting, Twisting and Sub-Optimal) controlling the FCGS are presented in Figs. 4.13, 4.14, 4.15 and 4.16. Numerical values of the controllers parameters are summarized in Appendix A, Table A.3. The former corresponds to the undisturbed system and depicts a magnified view of the time response of the sliding variable after the first step of current demand occurred (a brief lapse between 2 and 2.5 sec is displayed). Figure 4.14 shows the associate trajectories in the phase plane. The typical reaching behaviors of the three algorithms are manifested in this figure. It is observed that the three SOSM controllers display the expected finite-time convergence during this first part of the tests, with neither disturbances nor uncertainties present in the system.

Next, prior to the incorporation of the whole model uncertainties and external disturbances, it is of interest to appreciate the behavior of the control algorithms under the effect of measurement noise. To this end, between $t = 4$ sec and $t = 11$ sec important measurement noise is added to W_{cp}.

After that, from $t = 15$ to $t = 30$ sec, the FCGS is strongly perturbed by incorporating the compressor disturbance torque (given in (4.43), Fig. 4.4), together with all the parameter uncertainties of Table 4.1.

Figure 4.15 presents the actual and measured (noise included) W_{cp} time evolution of the FCGS controlled with the SOSM algorithms (for the sake of clarity, in this
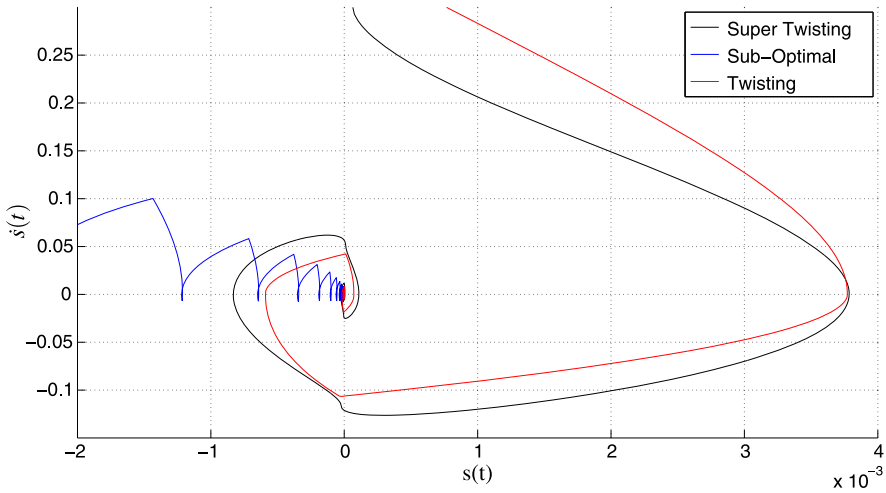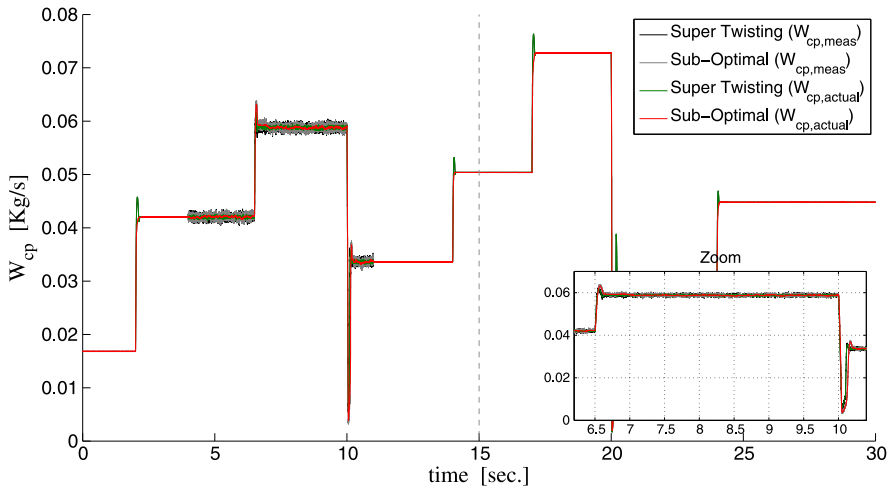
Fig. 4.14 $s(x)$ vs. $\dot{s}(x)$

Fig. 4.15 Compressor air mass flow

figure only the Super-Twisting and Sub-Optimal algorithms are depicted. In fact, the response of the Twisting controller would almost overlap the Super-Twisting one). Their performance can be assessed from the actual W_{cp} curves, proving all of them to have an excellent behavior. This is specially manifested after $t = 15$ sec, with the perturbations disturbing the system simultaneously.

Note that there is an output that can be considerably influenced by the measurement noise in certain cases. This is the net power of the generation system. Even though the latter has not been defined as an output from the strict control viewpoint,
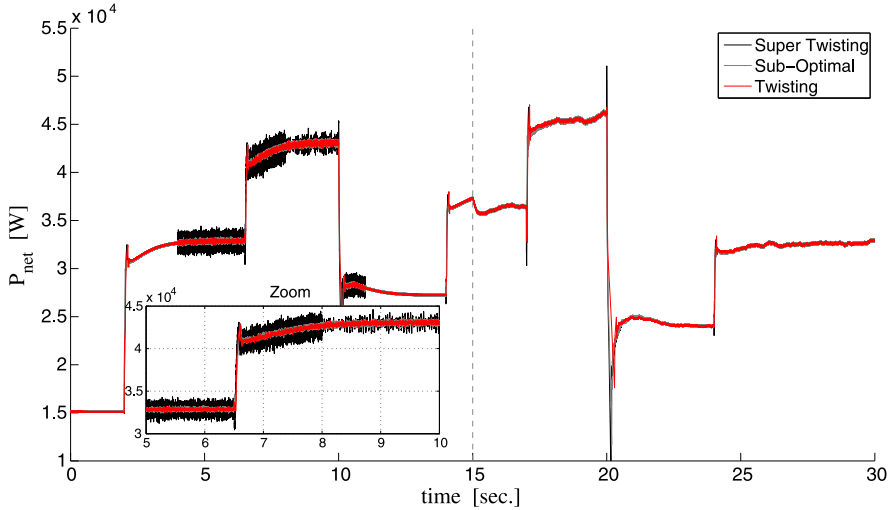
Fig. 4.16   FCGS net power

it is still an important physical output. Its sensitivity to high-frequency variations in the control input is because P_{net} has relative degree 0 with respect to u. In Fig. 4.16, it can be seen that the Super-Twisting algorithm may produce a more marked noise transmission to P_{net} than the other algorithms. This is clearly due to the fact that this algorithm contains a term related to s, not integrated, which directly injects the fluctuations of s into u.

Nevertheless, this is not necessarily a serious drawback for the algorithm application, since that negative effect can be considerably ameliorated with a proper tuning of λ. To illustrate this feature, the value of λ has been changed from 3 to 1.5 in the interval 8 sec $< t <$ 10 sec. In the zoom window in Fig. 4.16, a substantial reduction of the noise effect can be appreciated.

In the other two algorithms, measurement noise in s has been attenuated more in the P_{net} value since, in the relative degree 1 FCGS under consideration, the control terms that directly depend on s are integrated before entering to the plant.

4.7.2 LQR Controller

It is also interesting to establish comparisons between the proposed SOSM solutions and other more widely accepted techniques, such as state feedback linear control. To this end, a Linear Quadratic Regulator (LQR) controller proposed in [7, 8] is considered and analyzed in this subsection. As it can be appreciated in the cited bibliography, satisfactory results controlling the FCGS under study have been attained with this approach. In particular, this linear controller combines feedforward with
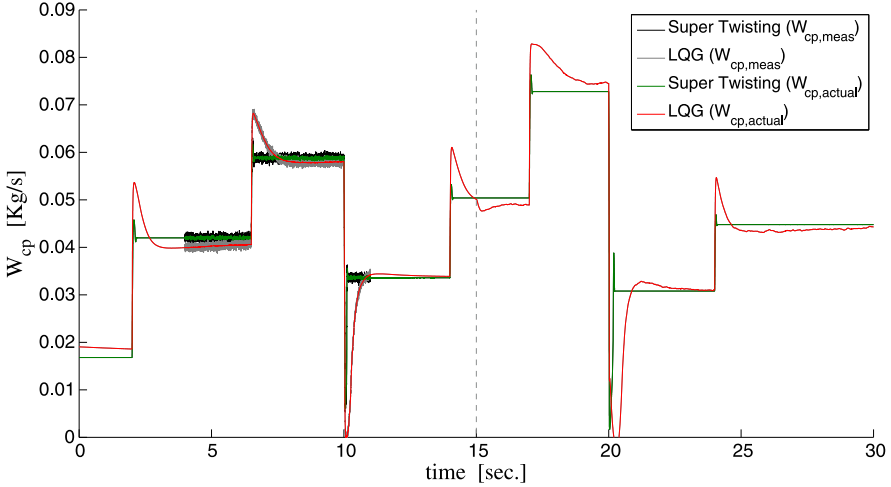
Fig. 4.17 Compressor air mass flow

feedback (state estimated plus integral) control. The form of the proposed controller
is [8]

$$V_{cp_i} = V_{cp_{ff}} + V_{cp_{LQR}} = V_{cp_{ff}} + V_{cp_p} - k \cdot \delta\hat{x}' - k_I \cdot q \qquad (4.48)$$

The implemented control input V_{cp_i} is the compressor voltage command, while
$V_{cp_{ff}}$ and V_{cp_p} are feedforward and pre-compensation terms, respectively, which
only depend on the measurable stack current I_{st}. The third term is a state feedback
control action, where $\delta\hat{x}'$ is the estimate of the linearized system state $\delta x' = x' - x'^o$.
The constant vector x'^o represents the state value at the nominal operating point of
linearization, in this case computed at optimal stoichiometry and a net power of
40 kW, with $I_{st} = 191$ A and $V_{cp} = 164$ V. Note that in this controller, the system
state x' has order eight, due to the additional presence of $m_{H_2,an}$ and $m_{w,an}$, the
mass of hydrogen and water inside the anode, respectively:

$$x' = [m_{O_2,ca} \quad m_{H_2,an} \quad m_{N_2,ca} \quad \omega_{cp} \quad P_{sm} \quad m_{sm} \quad m_{w,an} \quad P_{rm}]^T \quad (4.49)$$

The state estimation $\delta\hat{x}'$ is obtained using the Kalman-based observer presented
in [7]. The fourth term in (4.48) provides the integral control action, where the state
equation of the integrator is given by the compressor flow error:

$$\dot{q} = W_{air,ref} - W_{cp} \qquad (4.50)$$

Finally, the gains of the feedback control terms have been designed using LQR
optimal control techniques, resulting in [7]

$$k = \begin{bmatrix} -28.59 & -1.6 \times 10^{-13} & -60.57 & 7.57 & 579.74 & 2.55 \\ -3.6 \times 10^{-14} & -189.97 \end{bmatrix} \qquad (4.51)$$
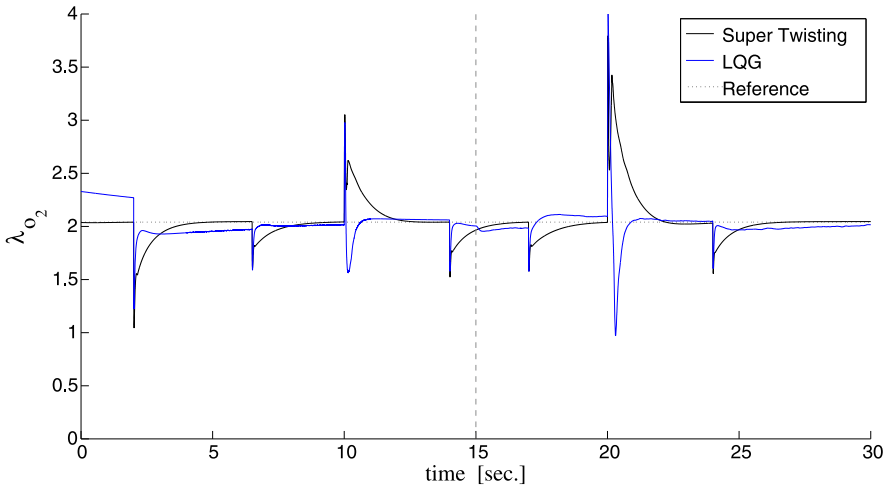
$$k_I = -0.18$$

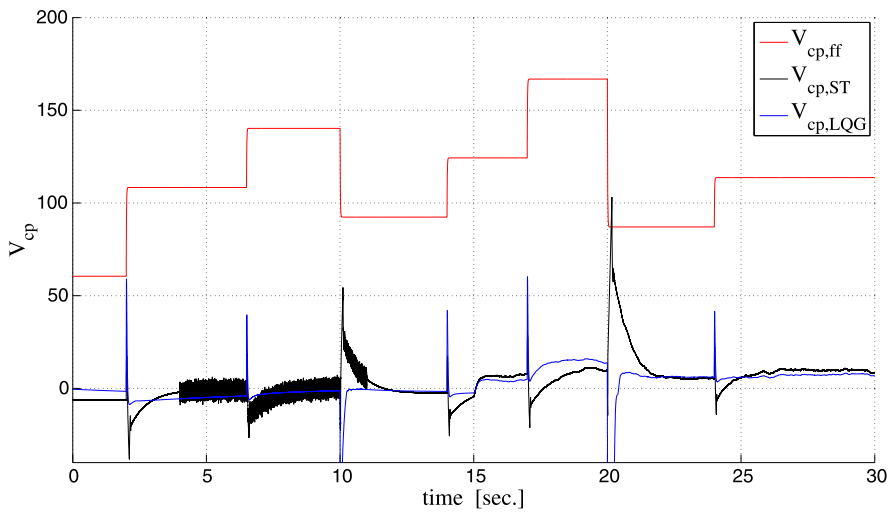**Fig. 4.18** Oxygen excess ratio (oxygen stoichiometry)

Fig. 4.19 Control action (in terms of the input voltage)

4.7.2.1 LQR Comparison Simulation Tests

For comparisons, the simulation tests presented in Figs. 4.17, 4.18 and 4.19 have been conducted under operating conditions similar to the ones in the previous subsections. Numerical values of the LQG controller parameters are summarized in Appendix A, Table A.4. They show the time evolution of the LQR and the Super-Twisting controlled system variables W_{cp} (actual and measured, with added noise), λ_{O_2} and the control actions (in terms of the input voltage), respectively.
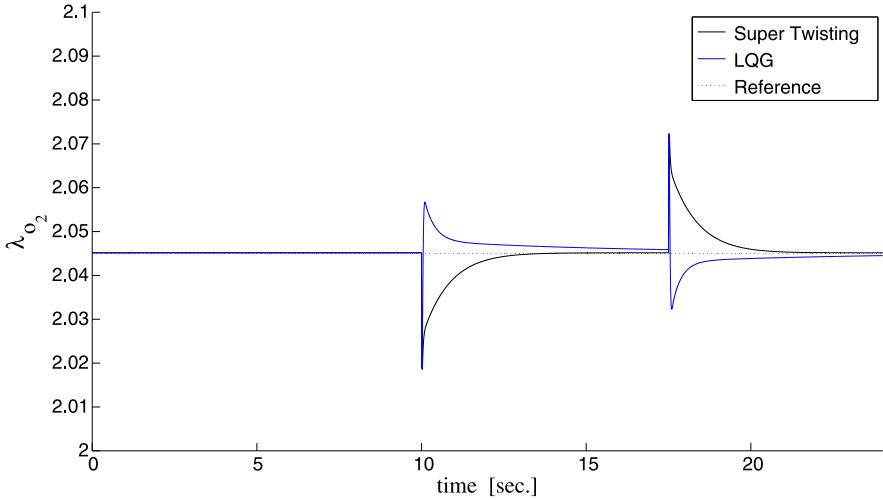
Fig. 4.20 Oxygen excess ratio (small excursion)

In the former figure, it can be appreciated that, during undisturbed operation, both controllers display very good results, although the Super-Twisting better regulates the actual W_{cp} at its desired value, given that it maintains $s = 0$ (recall Fig. 4.9), except for the abrupt steps of current I_{st}.

Respectively, with regard to the undisturbed behavior of the oxygen stoichiometry λ_{O_2}, it is observed in Fig. 4.18 that the LQR presents an initially faster dynamic response after the steeps, but in the end it requires longer times to reach the immediate vicinity of the desired value. On the other hand, the Super-Twisting controller attains less than 1% error in 3 sec.

It is worthwhile to mention that the linear LQR improves considerably its performance in the neighborhood of the linearization point. Moreover, in that region and considering small excursions, it could even surpass the performance of the Super-Twisting regarding the control of λ_{O_2} (see Fig. 4.20). However, as it can be observed in Figs. 4.17 and 4.18, the SOSM Super-Twisting excels the linear controller when working in a wide operation range.

Nevertheless, in this fuel cell application, it is in the presence of perturbations and uncertainties that the SOSM controller demonstrates its superiority over the LQR. This can be attested by comparing the response of both controllers under disturbed conditions (see $t > 15$ sec in Figs. 4.17 and 4.18).

To emphasize this feature, showing that the robustness of the Super-Twisting algorithm surpasses that of the LQR approach, a test conducted at constant $I_{st} = 191$ A (i.e., the value used for the linearized design of the LQR) is presented in Fig. 4.21. In this magnified view, the excellent robustness of the SOSM proposed controller can be clearly appraised.

To farther prove its advantageous robustness, a more exacting condition is introduced in Figs. 4.22 and 4.23, where the controllers are facing an extreme torque
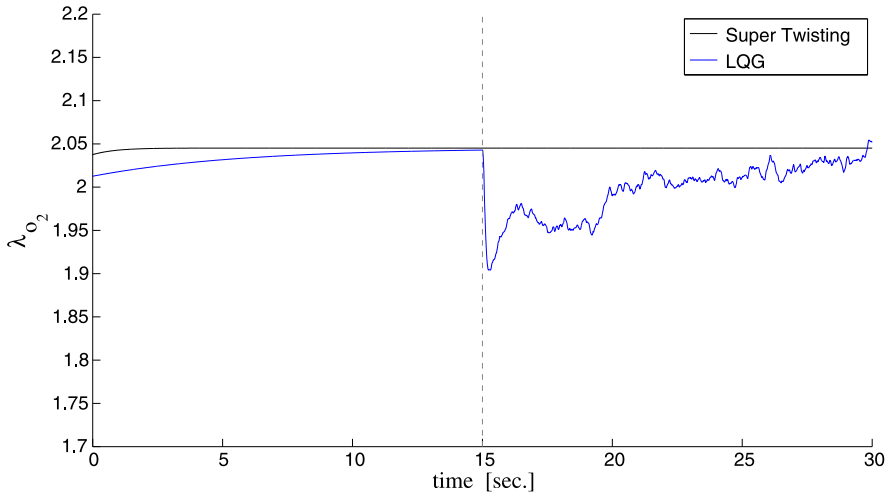
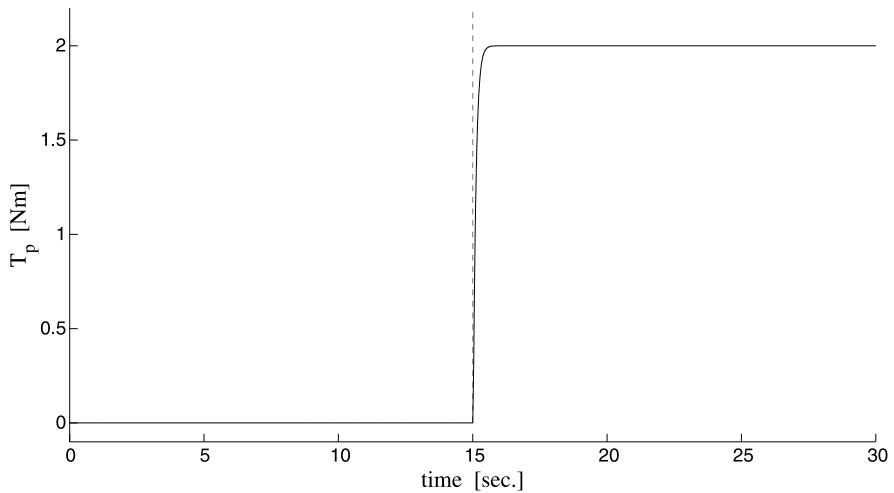**Fig. 4.21** Oxygen excess ratio (oxygen stoichiometry)

Fig. 4.22 Torque disturbance

disturbance (four times greater than the original). Even when subjected to this bulk disturbance, the Super-Twisting controller exhibits a remarkable robustness. Comparable satisfactory results have been obtained with the other SOSM controllers.

To conclude, it is interesting to stress that the Super-Twisting controller does not require of a state observer depending only on measurements, and its on-line computational burden is considerably lower.
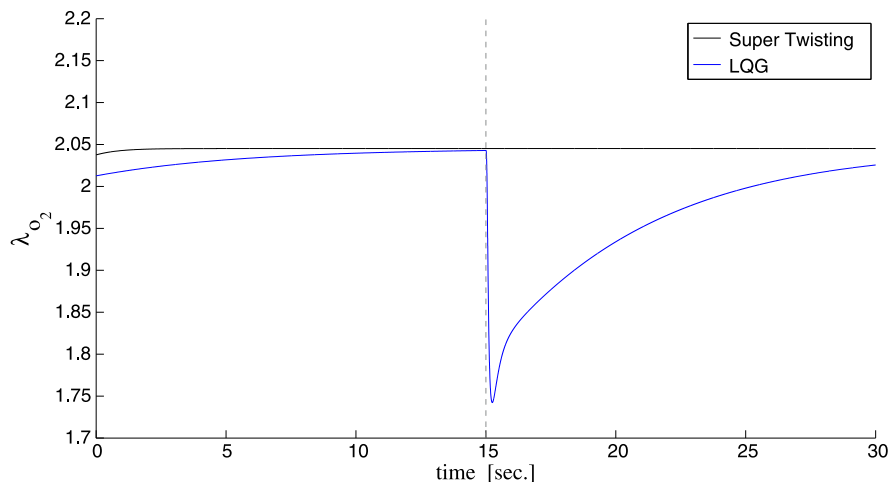
Fig. 4.23 Oxygen excess ratio (oxygen stoichiometry)

4.8 Conclusions

In this chapter the feasibility of SOSM techniques to control PEM fuel cells has been assessed. The evaluation has been conducted using a benchmark model of a fuel cell system for an electric vehicle. The analysis has established the viability of SOSM techniques for oxygen stoichiometry control, aiming to improve the overall energy efficiency.

Taking into account several features, such as the controlled system performance, robustness and implementation simplicity, the SOSM controllers are shown to be a highly efficient solution for this challenging problem, proving to be capable to robustly tracking the optimal air mass flow, even in the presence of severe external perturbations and model uncertainties. Among them, the Super-Twisting has been considered as a very suitable algorithm for the FCGS, given that it is specially intended for relative degree 1 systems and only requires the real-time knowledge of the sliding variable and not of its derivative.

Compared to the standard LQR control, the SOSM controllers demonstrate better robustness features, in a wide range of operation. Additionally, no state observers are required, resulting in a simple and low-computational-cost algorithm.

Now that the suitability of SOSM control for FCGS has been confirmed, the following stage will be the development and implementation of these controllers in an experimental fuel cell plant. This will be the subject matter of the following two chapters.

References

1. Arce A (2010) Advanced control for fuel cell systems. PhD thesis, Universidad de Sevilla

2. Boyce M (1982) Gas turbine engineering handbook. Gulf, Houston
3. Gravdahl J, Egeland O (1999) Compressor surge and rotating stall. Springer, London
4. Kunusch C (2006) Second order sliding mode control of a fuel cell stack using a twisting algorithm. Master thesis, Electrical Department, National University of La Plata, Argentina (in Spanish)
5. Kunusch C, Puleston P, Mayosky M, Riera J (2009) Sliding mode strategy for PEM fuel cells stacks breathing control using a super-twisting algorithm. IEEE Trans Control Syst Technol 17:167–174
6. Moraal P, Kolmanovsky I (1999) Turbocharger modeling for automotive control applications. SAE Technical Paper 1999-01-0908
7. Pukrushpan J, Stefanopoulou A, Peng H (2004) Control of fuel cell breathing. IEEE Control Syst Mag 24(2):30–46
8. Pukrushpan J, Stefanopoulou A, Peng H (2004) Control of fuel cell power systems. Springer, Berlin
9. Rodatz P (2003) Dynamics of the polymer electrolyte fuel cell: experiments and model-based analysis. PhD thesis, Swiss Federal Institute of Technology Zurich
10. Springer T, Zawodzinski T, Gottesfeld S (1991) Polymer electrolyte fuel cell model. J Electrochem Soc 138(8):2334–2342